

University of California - Davis
University of Wisconsin - Madison

UCD-96-19
MADPH-96-949
IUHET-336
June 1996

Studying a Strongly Interacting Electroweak Sector via Longitudinal Gauge Boson Scattering at a Muon Collider

V. Barger^a, M.S. Berger^b, J.F. Gunion^c, T. Han^c,

^a*Physics Department, University of Wisconsin, Madison, WI 53706, USA*

^b*Physics Department, Indiana University, Bloomington, IN 47405, USA*

^c*Physics Department, University of California, Davis, CA 95616, USA*

Abstract

We discuss the excellent prospects for a detailed study of a strongly interacting electroweak sector at a muon collider with c.m. energy $\sqrt{s} \sim 4$ TeV. For expected luminosity of $L = 200 - 1000 \text{ fb}^{-1}$ per year, $\mu^+\mu^-$ and $\mu^+\mu^+$ (or $\mu^-\mu^-$) collisions can be used to study longitudinal W^+W^- and W^+W^+ (or W^-W^-) scattering with considerable precision. In particular, detailed measurements of the distribution in the VV pair masses ($V = W^\pm, Z$) will be possible. The shape and magnitude of these distributions will provide a powerful tool for determining the nature of strong gauge boson interactions. Event rates will be large enough that projection techniques can be used to directly isolate final states with different polarizations of the V 's and verify that the strong interaction cross section excess is mainly in the longitudinal-longitudinal mode.

1 Introduction

Despite the extraordinary success of the Standard Model (SM) in describing particle physics up to the highest energy available today, the nature of electroweak symmetry-breaking (EWSB) remains undetermined. In particular, it is conceivable that there is no light ($\lesssim 700$ GeV) Higgs boson. General arguments [1] based on partial wave unitarity then imply that the W^\pm, Z electroweak gauge bosons develop strong (non-perturbative) interactions by energy scales of order 1–2 TeV. For a collider to probe such energy scales, the c.m. energy must be sufficient that gauge-boson scattering (see Fig. 1) at subprocess energies at or above 1 TeV occurs with substantial frequency. The only colliders under construction or being planned that potentially meet this requirement are the CERN LHC, a next linear e^+e^- collider (NLC, with $\sqrt{s} \lesssim 1.5$ TeV), and a high energy muon collider (NMC).

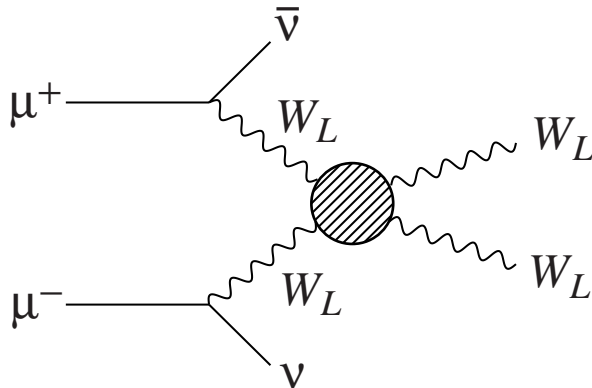


Figure 1: Symbolic diagram for strong VV scattering.

The ability to extract signals and learn about a strongly-interacting-electroweak sector (SEWS) at the LHC and NLC has been the subject of many studies [2,3,4,5,6]. The conclusion is that the LHC and NLC will yield first evidence for a SEWS theory, but for many models the evidence will be of rather marginal statistical significance. SEWS models yielding large signals (such as the Standard Model with a 1 TeV Higgs boson or a model with a spin-1, isospin-1 resonance at 1 TeV) will be readily apparent or easily eliminated, but models that yield only a small number of excess events will be very difficult to distinguish from one another. Measurement of the VV mass spectrum

(here we generically denote W^\pm, Z by V), would reveal a wealth of information about SEWS models, but is not feasible at the LHC or NLC.

Our focus in this paper is the ability of a muon collider to distinguish between and perform detailed studies of SEWS models for longitudinal gauge-boson scattering. There may be additional large and easily observed signals in dynamical symmetry breaking models; for example, in Technicolor models both Technicolor hadrons [7] and techni-rho resonances [8,9] would be easily detected whenever the energy is adequate for them to be produced at a reasonable rate. Only the SEWS signals are addressed in the present work.

We shall demonstrate that a muon collider with center-of-mass energy, \sqrt{s} , of order 4 TeV would allow a comprehensive study of the M_{VV} distributions in all channels, assuming (as should be the case) that $\mu^+\mu^-$ and $\mu^+\mu^+$ (or $\mu^-\mu^-$) collisions are possible at the planned luminosity of $L \sim 200 - 1000 \text{ fb}^{-1}$ per year. A c.m. energy of $\sqrt{s} = 3 - 4 \text{ TeV}$ is the smallest that will allow such a detailed study. Construction of a multi-TeV e^+e^- collider might also be a possibility [10], and would provide similar capabilities if an e^-e^- facility is included, although bremsstrahlung-photon-initiated backgrounds would be larger than at the muon collider.

In order to isolate the SEWS signals, it is necessary to determine if there are events in the $\nu\bar{\nu}VV$ final states at large M_{VV} due to strong scattering of V 's with longitudinal (L) polarization beyond those that will inevitably be present due to standard electroweak processes, including VV scattering, that primarily produce V 's with transverse (T) polarization. There are two obvious ways of determining if such events are present.

- The first is to look for an excess of events beyond what is expected in the Standard Model when the Higgs boson is light and there is no strong scattering. This involves reliably computing the irreducible and reducible SM ‘backgrounds’ and subtracting them from the observed rates.
- The second is to employ projection techniques to separately isolate the V_LV_L , V_TV_T and V_TV_L contributions.

Only the first procedure is practical at the LHC and NLC (with $\sqrt{s} \lesssim 1.5 \text{ TeV}$) because of limited event rates. The Standard Model with a light Higgs boson of mass $m_H = 100 \text{ GeV}$ is used to define the irreducible background, and will be denoted by

“LH”.^{*} This definition of the irreducible background is appropriate since the growth in the VV event rate in going from small m_H to large m_H (or because of some other SEWS model) is almost entirely due to an increase in the $V_L V_L$ rate, the $V_T V_T$ and $V_T V_L$ rates being essentially independent of m_H . Thus, the SEWS signal is given by

$$\frac{d\Delta\sigma(\text{SEWS})}{dM_{VV}} \equiv \frac{d\sigma(\text{SEWS})}{dM_{VV}} - \frac{d\sigma(\text{LH})}{dM_{VV}}, \quad (1)$$

with $\Delta\sigma(\text{SEWS})$ being the integral thereof over a specified range of M_{VV} .

At a 4 TeV muon collider, the subtraction procedure yields dramatic signals. Further, the projection technique for isolating the longitudinal V_L scattering rates becomes very practical and exploration for new physics beyond the SM becomes possible in all three polarization channels — TT , LL and TL — independently. As previously emphasized, in SEWS models the new strong interactions affect only the LL (and, in some cases, the TL) sector, and not the TT sector. However, theories predicting large anomalous couplings could yield TT rates that also differ from SM expectations, and this difference could be uncovered by the polarization analysis.

2 Overview of Models

Numerous models for the strongly interacting gauge sector have been considered. We focus on a selection of those considered in Ref. [2]:

- the Standard Model with a heavy Higgs boson of mass $m_H = 1$ TeV;
- a (“Scalar”) model in which there is a spin-0, isospin-0 resonance with $M_S = 1$ TeV but non-SM width of $\Gamma_S = 350$ GeV;
- a (“Vector”) model in which there is a spin-1, isospin-1 vector resonance with either $M_V = 1$ TeV and $\Gamma_V = 35$ GeV or $M_V = 2$ TeV and $\Gamma_V = 0.2$ TeV, but no spin-0 resonance. When necessary, we unitarize the model using K -matrix techniques as detailed in the Appendix.
- a model, denoted by LET-K or “ $m_H = \infty$ ”, in which the SM Higgs is taken to have infinite mass and the partial waves simply follow the behavior predicted

^{*}We note that the specific choice of m_H is not material so long as it is well below the vector-boson pair threshold.

by the low-energy theorems, except that the LET behavior is unitarized via the K -matrix techniques described in the Appendix.

We note that the $m_H = 1$ TeV Standard Model is the simplest VV scattering model for which the full kinematics and spin correlations among the final decay products are easily calculable. Consequently, this model is extremely useful in bench mark studies of the effectiveness of cuts and projection techniques. As discussed in Ref. [2], the distributions of the final V_L 's, and their decay products, in other models should follow closely those found for the V_L 's in the $m_H = 1$ TeV Standard Model. Thus, in analyzing the other SEWS models, we assume that cut efficiencies and distributions are the same as for the $m_H = 1$ TeV SM V_L 's.

Each distinct SEWS model yields a definite form for the fundamental amplitude $A(s, t, u)$ defined by the weak isospin decomposition:

$$\mathcal{M}(W_L^a W_L^b \rightarrow W_L^c W_L^d) = A(s, t, u) \delta^{ab} \delta^{cd} + A(t, s, u) \delta^{ac} \delta^{bd} + A(u, t, s) \delta^{ad} \delta^{bc}, \quad (2)$$

where $a, b, c, d = 1, 2, 3$, with $W_L^\pm = (1/\sqrt{2})(W_L^1 \mp iW_L^2)$ and $Z_L = W_L^3$. All the physics of $V_L V_L$ scattering is contained in the amplitude function $A(s, t, u)$.

The physical amplitudes for boson-boson scattering processes of interest are as follows:

$$\mathcal{M}(W_L^+ W_L^- \rightarrow Z_L Z_L) = A(s, t, u) \quad (3)$$

$$\mathcal{M}(W_L^+ W_L^- \rightarrow W_L^+ W_L^-) = A(s, t, u) + A(t, s, u) \quad (4)$$

$$\mathcal{M}(W_L^\pm Z_L \rightarrow W_L^\pm Z_L) = A(t, s, u) \quad (5)$$

$$\mathcal{M}(W_L^\pm W_L^\pm \rightarrow W_L^\pm W_L^\pm) = A(t, s, u) + A(u, t, s). \quad (6)$$

These expressions for the amplitudes do not include the symmetry factors for identical particles. The isospin amplitudes T_I , for isospin I , are given by

$$T_0 = 3A(s, t, u) + A(t, s, u) + A(u, t, s), \quad (7)$$

$$T_1 = A(t, s, u) - A(u, t, s), \quad (8)$$

$$T_2 = A(t, s, u) + A(u, t, s). \quad (9)$$

In terms of the T_I , the relevant physical scattering amplitudes can be written as

$$\mathcal{M}(W_L^+ W_L^- \rightarrow Z_L Z_L) = \frac{1}{3}[T_0 - T_2] \quad (10)$$

$$\mathcal{M}(W_L^+ W_L^- \rightarrow W_L^+ W_L^-) = \frac{1}{6}[2T_0 + 3T_1 + T_2] \quad (11)$$

$$\mathcal{M}(W_L^\pm Z_L \rightarrow W_L^\pm Z_L) = \frac{1}{2}[T_1 + T_2] \quad (12)$$

$$\mathcal{M}(W_L^\pm W_L^\pm \rightarrow W_L^\pm W_L^\pm) = T_2. \quad (13)$$

Again, these amplitudes do not include the identical particle symmetry factors.

Measurements of the processes

$$\begin{aligned} W^+ W^- &\rightarrow W^+ W^-, ZZ, \\ W^\pm Z &\rightarrow W^\pm Z, \\ W^\pm W^\pm &\rightarrow W^\pm W^\pm, \end{aligned} \quad (14)$$

as a function of s , t , and u provide as much information on the T_I and the function $A(s, t, u)$ as can be accessed experimentally. A full reconstruction of the T_I , including phases, is not possible since the cross sections depend upon the amplitudes of Eqs. (10-13) squared. If it is necessary to integrate over the s, t, u variables in order to obtain statistically significant measurements, then much information is lost.

As shown below, a 4 TeV muon collider can provide at least a reasonably good determination of the M_{VV} invariant mass spectrum for each of the above reactions. In contrast, for most models, the LHC or a $\sqrt{s} \lesssim 1.5$ TeV NLC can at best allow determination of integrals over broad ranges of M_{VV} .

3 Probing SEWS Models at the LHC and NLC

If the electroweak sector is strongly interacting, partial exploration of the underlying SEWS model in the three weak-isospin channels ($I = 0, 1, 2$) will be possible at the LHC. The signal and background for gold-plated (purely leptonic) events is shown in Table 1 for the LHC operating at 14 TeV with $L = 100 \text{ fb}^{-1}$, for several of the above models. These event rates were computed after imposing a series of crucial cuts required to suppress background and after integrating over a broad range of M_{VV} values (or effectively so for final states in which M_{VV} cannot be directly reconstructed). Discrimination among models is achieved by comparing the gold-plated event rates in the different channels. For example, if the signal rate is largest in the $W^\pm W^\pm$ like-sign channels, then non-resonant models such as the LET-K would be preferred. Similarly, a large $W^\pm Z$ signal relative to the ZZ and $W^\pm W^\pm$ channels

would favor a Vector resonance model. However, only in the case of the $M_V = 1$ TeV Vector model would there be any chance of actually observing details regarding the structure of the M_{VV} spectrum at the LHC. A $M_V = 2$ TeV Vector model would be virtually indistinguishable from the LET-K model.

Table 1: Total numbers of $V_L V_L \rightarrow 4\text{-lepton}$ signal S and background B events calculated for the LHC [2], assuming $L = 100 \text{ fb}^{-1}$. The Vector model is that with $M_V = 1$ TeV and $\Gamma_V = 35$ GeV. The Scalar model has $M_S = 1$ TeV, $\Gamma_S = 350$ GeV.

	Bkgd	Scalar	Vector	LET-K
$ZZ(4\ell)$	1	5	1.5	1.5
$(2\ell 2\nu)$	2	17	5	4.5
W^+W^-	12	18	6	5
W^+Z	22	2	70	3
$W^\pm W^\pm$	4	7	12	13

The channels and models in Table 1 have also been studied for a 1.5 TeV NLC [5]. As illustrated in Table 2, event rates in the (usable) four jet final states are more promising than in the purely leptonic final states at the LHC. The rates are at a level that SEWS models with large signals, such as the $m_H = 1$ TeV SM or $m_V = 1$ TeV Vector model, would be apparent, but detecting the signals for models without dramatic resonances, such as the LET-K model, would be difficult. It would also not be possible to distinguish the $m_H = 1$ TeV model from a Scalar model with narrower resonance width. Detailed study of the strong interactions through the M_{VV} distributions would not be possible.

4 Rates and Motivations for Higher Energy

For a first estimate of the strong electroweak scattering effects we take the Standard Model with a heavy Higgs as a prototype of the strong scattering sector. For a 1 TeV SM Higgs boson, the SEWS signal is accordingly defined as

$$\Delta\sigma = \sigma(m_H = 1 \text{ TeV}) - \sigma(\text{LH}) . \quad (15)$$

Results in the W^+W^- and ZZ channels for $\Delta\sigma$ (with no cuts of any kind) are shown in Table 3 for $\sqrt{s} = 1.5$ TeV (as often discussed for an e^+e^- collider) and 4 TeV.

Table 2: Total numbers of W^+W^- , $ZZ \rightarrow 4\text{-jet}$ signal S and background B events calculated for a 1.5 TeV NLC with integrated luminosity 200 fb^{-1} , using 100% polarized e_L^- beams [5]. Events are summed over the mass range $0.5 < M_{WW} < 1.5 \text{ TeV}$ except for the W^+W^- channel with a narrow vector resonance in which $0.9 < M_{WW} < 1.1 \text{ TeV}$. The statistical significance S/\sqrt{B} is also given. For comparison, results for $e^-e^- \rightarrow \nu\nu W^-W^-$ are also presented, for the same energy and luminosity and the W^+W^- cuts. The hadronic branching fractions of WW decays and the W^\pm/Z identification/misidentification are included.

channels	SM $m_H = 1 \text{ TeV}$	Scalar $M_S = 1 \text{ TeV}$	Vector $M_V = 1 \text{ TeV}$	LET-K
$S(e^+e^- \rightarrow \bar{\nu}\nu W^+W^-)$	330	320	92	62
$B(\text{backgrounds})$	280	280	7.1	280
S/\sqrt{B}	20	20	35	3.7
$S(e^+e^- \rightarrow \bar{\nu}\nu ZZ)$	240	260	72	90
$B(\text{backgrounds})$	110	110	110	110
S/\sqrt{B}	23	25	6.8	8.5
$S(e^-e_L^- \rightarrow \nu\nu W^-W^-)$	54	70	72	84
$B(\text{background})$	400	400	400	400
S/\sqrt{B}	2.7	3.5	3.6	4.2
$S(e_L^-e_L^- \rightarrow \nu\nu W^-W^-)$	110	140	140	170
$B(\text{background})$	710	710	710	710
S/\sqrt{B}	4.0	5.2	5.4	6.3

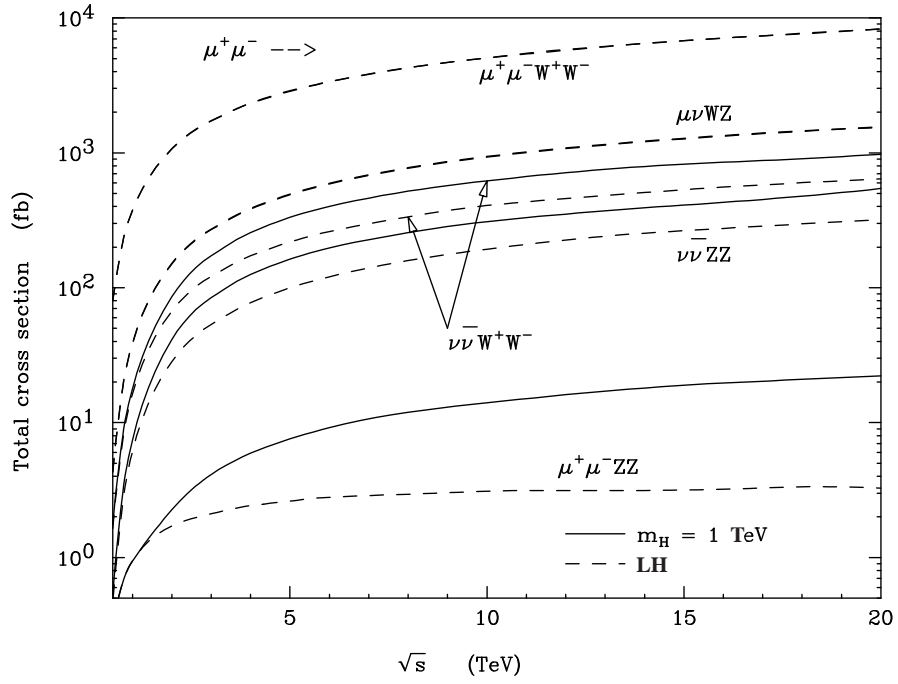


Figure 2: Signal and background cross sections as a function of \sqrt{s} for strong $W^+W^- \rightarrow W^+W^-$ and $W^+W^- \rightarrow ZZ$ scattering as computed in the SM for $m_H = 1$ TeV at a $\mu^+\mu^-$ collider.

The strong scattering signal is relatively small at energies of order 1 TeV, but grows substantially as multi-TeV energies are reached. This is illustrated in Fig. 2, where $\sigma(m_H = 1 \text{ TeV})$ and $\sigma(\text{LH})$ are plotted separately. The signal $\Delta\sigma$ declines rapidly in magnitude for decreasing energy below $\sqrt{s} = 4 \text{ TeV}$. The associated signal (S) and irreducible background event rates are given by $S = L\Delta\sigma$ and $L\sigma(\text{LH})$, where L is the integrated luminosity. Table 3 shows that a very respectable signal rate is achieved at 4 TeV and even before cuts the signal to irreducible background ratio is quite reasonable; both are much larger than at $\sqrt{s} = 1.5 \text{ TeV}$. SEWS physics benefits from increasing energy in four ways.

- The luminosity for $V_L V_L$ collisions is bremsstrahlung-initiated and grows at fixed subprocess $\hat{s} = M_{VV}^2$ as $1/\tau$ where $\tau = M_{VV}^2/s$.
- The SEWS amplitude function $A(\hat{s}, \hat{t}, \hat{u})$ typically increases as higher subprocess $\hat{s} = M_{VV}^2$ values become accessible; *e.g.* in the LET-K model $A(\hat{s}, \hat{t}, \hat{u}) \propto \hat{s}/v^2$, where v is the standard electroweak symmetry breaking parameter. This more than compensates for the slightly faster growth with s of the $V_T V_T$ luminosity function (responsible for VV fusion backgrounds) $\propto \frac{1}{\tau} \ln^2 \frac{s}{m_V^2}$ as compared to the $V_L V_L$ luminosity.
- The background subprocess amplitudes typically have point-like $1/\hat{s}$ behavior and, further, some backgrounds are not proportional to the growing VV luminosities. In particular, many of the diagrams contributing to the amplitude for the irreducible light Higgs $V_T V_T + V_T V_L$ SM background do not have VV fusion topology.
- Finally, the luminosities at higher machine energies are normally designed to be larger to compensate for the $1/\hat{s}$ decline of the point-like subprocess cross sections for other types of new physics.

It appears that $\sqrt{s} = 4 \text{ TeV}$ is roughly the critical energy at which SEWS physics can first be studied in detail. This is especially true given that it will be desirable to impose strong cuts in order to maximize signal over background. Thus, the high energy reach of a muon collider could prove to be critically important.

The importance of high energy and signal selection cuts is particularly apparent in the $W^+ W^+$ channel. We choose this channel to illustrate the polarization structure

Table 3: Strong electroweak scattering signals in $W^+W^- \rightarrow W^+W^-$ and $W^+W^- \rightarrow ZZ$ at future lepton colliders. Signal cross sections and the signal to irreducible LH background ratio are given for $L = 200 \text{ fb}^{-1}$ at $\sqrt{s} = 1.5 \text{ TeV}$ and $L = 1000 \text{ fb}^{-1}$ at $\sqrt{s} = 4 \text{ TeV}$, with no cuts.

\sqrt{s}	$\Delta\sigma(W^+W^-)$	$[S/\text{LH}](W^+W^-)$	$\Delta\sigma(ZZ)$	$[S/\text{LH}](ZZ)$
1.5 TeV	8 fb	$\frac{1600}{8000}$	6 fb	$\frac{1200}{3600}$
4 TeV	80 fb	$\frac{80000}{170000}$	50 fb	$\frac{50000}{80000}$

Table 4: Standard Model cross sections (in fb) at $\sqrt{s} = 4 \text{ TeV}$ in the W^+W^+ final state TT , TL and LL modes for a light Higgs compared to $m_H = 1 \text{ TeV}$. Results are given both without any cuts and after imposing cuts I and II on the W^+ 's as delineated in Section 4.

	LH				$m_H = 1 \text{ TeV}$			
	TT	TL	LL	Sum	TT	TL	LL	Sum
No Cuts	48.9	26.9	6.75	82.6	49.5	26.5	12.1	88.1
With Cuts	1.34	0.19	0.03	1.56	1.36	0.15	1.51	3.02

of the VV final state. In Table 4 we compare the polarization decomposition of the Standard Model W^+W^+ cross sections for the LH case with the $m_H = 1 \text{ TeV}$ SEWS model. (We define the vector boson polarizations in the VV rest frame.) With no cuts, substantial TL and not insignificant LL cross section components are present for the LH model, in addition to the dominant TT cross section. The increase ($\Delta\sigma$) in cross section in going to $m_H = 1 \text{ TeV}$ is a small percentage of the total and is seen to be almost entirely in the LL final state (the TL contribution actually decreases). By imposing cuts on the W^+ 's (specifically cuts I and II as delineated in Section 4), the TL and, especially, LL cross sections are reduced to negligible size compared to TT for the LH model. Further, with the cuts imposed, $\Delta\sigma$ is nearly as large as $\sigma(\text{LH})$. Thus, cuts are important both in reducing the background relative to the signal and also in isolating the LL component of the strongly interacting gauge boson cross section. Whether cuts are imposed or not, it is clear from Table 4 that the TT contribution to $\Delta\sigma$ is negligible. Finally, the magnitude of $\Delta\sigma$ in the W^+W^+ channel (even before cuts) becomes sufficient at $\sqrt{s} = 4 \text{ TeV}$ to allow quantitative study; for $\sqrt{s} \lesssim 1.5 \text{ TeV}$ $\Delta\sigma$ is so small that the W^+W^+ channel can at best provide only a hint of strong interactions among the gauge bosons.

5 Muon Collider Results using the Subtraction Procedure

For a $\mu^+\mu^-$ collider operating at 4 TeV the event rates and statistical significances for most channels markedly improve, the exception being the $W^\pm Z \rightarrow W^\pm Z$ channel. Table 5 summarizes our results for various SEWS models in the $W^+W^- \rightarrow W^+W^-$, $W^+W^- \rightarrow ZZ$ and $W^+W^+ \rightarrow W^+W^+$ channels[†] for the signal S and the full irreducible plus reducible background B event numbers obtained by summing over diboson invariant mass bins as specified in the caption. Also given is the statistical significance, S/\sqrt{B} , of the signals. The signal rate S is computed by subtracting the background rate B from the total event rate (signal+background) for a given SEWS model, see Eq. (15). The results presented in Table 5 are those obtained after imposing the following cuts:

- I: Basic Cuts: $p_T(V) \geq 150$ GeV; $|\cos \theta_V| \leq 0.8$; $M_{VV} \geq 500$ GeV;
- II: $20 \text{ GeV} \leq p_T(ZZ) \leq 300 \text{ GeV}$; $30 \text{ GeV} \leq p_T(WW) \leq 300 \text{ GeV}$; and veto of any μ^\pm with $\theta_\mu \geq 12^\circ$ and $E_\mu \geq 50$ GeV (assuming the beam hole has a 12° opening);
- III: separation of W 's from Z 's in the 4-jet final state using the mass cuts in Eq. (16) below.

The $p_T(VV)$ cuts and muon veto in II are designed to suppress reactions such as $\mu^+\mu^- \rightarrow \mu^+\mu^-W^+W^-$ deriving from subprocesses involving initial state photons emitted from the incoming μ^+, μ^- . The veto eliminates a large fraction of such events. Further, the $V_L V_L$ signal tends to have $p_T(VV) \sim m_W$, whereas $p_T(VV)$ for the $\mu^+\mu^-W^+W^-$ final state is quite small, especially after the veto cut. In order to separate W 's from Z 's in the final state we define, following Ref. [5], a W , Z as two jets having invariant mass in the ranges

$$M_{jj}^W \in [0.85m_W, \frac{1}{2}(m_W + m_Z)], \quad M_{jj}^Z \in [\frac{1}{2}(m_W + m_Z), 1.15m_Z], \quad (16)$$

[†]We focus on the $W^+W^+ \rightarrow W^+W^+$ like-sign channel, but the same results apply to the $W^-W^- \rightarrow W^-W^-$ channel. High luminosity $\mu^+\mu^+$ collisions may be somewhat easier to achieve.

respectively. For a detector with resolution $\Delta E_j/E_j = 0.50/\sqrt{E_j} \oplus 0.02$, the true WW , WZ and ZZ final states will be interpreted statistically as follows:

$$\begin{aligned} WW &\Rightarrow 78\% WW, 18\% WZ, 1\% ZZ, 3\% \text{ reject}, \\ WZ &\Rightarrow 11\% WW, 77\% WZ, 9\% ZZ, 3\% \text{ reject}, \\ ZZ &\Rightarrow 7\% WW, 22\% WZ, 72\% ZZ, 4\% \text{ reject}. \end{aligned}$$

Misidentification of a WW final state as ZZ is especially unlikely.

Before turning to an examination of the M_{VV} distributions, we summarize the implications of the integrated event rates appearing in Table 5. Most importantly, the statistical significance of the SEWS signal is high for all channels, regardless of model. Even the $m_H = \infty$, W^+W^- and $m_H = 1$ TeV, W^+W^+ signals are clearly visible with only $L = 200 \text{ fb}^{-1}$, becoming thoroughly robust for $L = 1000 \text{ fb}^{-1}$. (Note that in this case the ratio S/B can be enhanced by making a higher mass cut (*e.g.* $M_{VV} > 0.7 \text{ TeV}$), but the significance S/\sqrt{B} is not improved.) Second, models of distinctly different types are easily distinguished from one another. A broad Higgs-like scalar will enhance both W^+W^- and ZZ channels with $\sigma(W^+W^-) > \sigma(ZZ)$; a ρ -like vector resonance will manifest itself through W^+W^- but not ZZ ; the unitarized $m_H = \infty$ (LET-K) amplitude will enhance ZZ more than W^+W^- .

The importance of the $p_T(VV)$ cut, the veto of energetic muons outside the beam hole and the mass cuts is illustrated by comparing Fig. 3 to Fig. 4. In Fig. 3, we plot the $m_H = 1 \text{ TeV}$ and unitarized $m_H = \infty$ signals, the irreducible LH background and the most important reducible backgrounds after imposing only the basic cuts I. Without the additional cuts II and III the reducible backgrounds are much more important than the irreducible $\nu\bar{\nu}W^+W^-$ and $\nu\bar{\nu}ZZ$ backgrounds. Also evident from this figure is the importance of unitarizing the $m_H = \infty$ partial wave behavior predicted in the SM. Without unitarization (the dotted histograms) there is an extensive (unphysical) tail at high M_{VV} . These histograms should be compared to the corresponding histograms in Fig. 4 obtained after imposing all the cuts, I-III. The dramatic reduction in the reducible backgrounds relative to the SEWS signals and the irreducible LH background in both the W^+W^- and ZZ channels offsets some sacrifice in the overall rate. The cuts were chosen in order to roughly maximize the statistical significances of different SEWS models as given in Table 5.

The channel $W^\pm Z \rightarrow W^\pm Z$ is less interesting than the W^+W^- , W^+W^+ and ZZ channels for the following reasons. First, there is no direct s -channel scalar

Table 5: Total numbers of W^+W^- , ZZ and $W^+W^+ \rightarrow 4\text{-jet}$ signal (S) and background (B) events calculated for a 4 TeV $\mu^+\mu^-$ collider with integrated luminosity 200 fb^{-1} (1000 fb^{-1} in the parentheses), for cuts of $M_{VV} \geq 500 \text{ GeV}$, $p_T(V) \geq 150 \text{ GeV}$, $|\cos \theta_V| \leq 0.8$ and $p_T(WW) \geq 30 \text{ GeV}$, $p_T(ZZ) \geq 20 \text{ GeV}$. (For the case of a 2 TeV vector state, events for the W^+W^- channel are summed around the mass peak over the range $1.7 < M_{VV} < 2.3 \text{ TeV}$.) Events containing a μ^+ or μ^- with $\theta_\mu \geq 12^\circ$ and $E_\mu \geq 50 \text{ GeV}$ are vetoed. The signal rate S is that obtained by computing the total rate (including all backgrounds) for a given SEWS model and then subtracting the background rate; see Eq. (15). The statistical significance S/\sqrt{B} is given for the signal from each model. The hadronic branching fractions of VV decays and the W^\pm/Z identification/misidentification are included.

channels	Scalar $m_H = 1 \text{ TeV}$ $\Gamma_H = 0.5 \text{ TeV}$	Vector $M_V = 2 \text{ TeV}$ $\Gamma_V = 0.2 \text{ TeV}$	LET-K $m_H = \infty$ Unitarized
$\mu^+\mu^- \rightarrow \bar{\nu}\nu W^+W^-$			
$S(\text{signal})$	2400 (12000)	180 (890)	370 (1800)
$B(\text{backgrounds})$	1200 (6100)	25 (120)	1200 (6100)
S/\sqrt{B}	68 (152)	36 (81)	11 (24)
$\mu^+\mu^- \rightarrow \bar{\nu}\nu ZZ$			
$S(\text{signal})$	1030 (5100)	360 (1800)	400 (2000)
$B(\text{backgrounds})$	160 (800)	160 (800)	160 (800)
S/\sqrt{B}	81 (180)	28 (64)	32 (71)
$\mu^+\mu^+ \rightarrow \bar{\nu}\bar{\nu} W^+W^+$			
$S(\text{signal})$	240 (1200)	530 (2500)	640 (3200)
$B(\text{backgrounds})$	1300 (6400)	1300 (6400)	1300 (6400)
S/\sqrt{B}	7 (15)	15 (33)	18 (40)

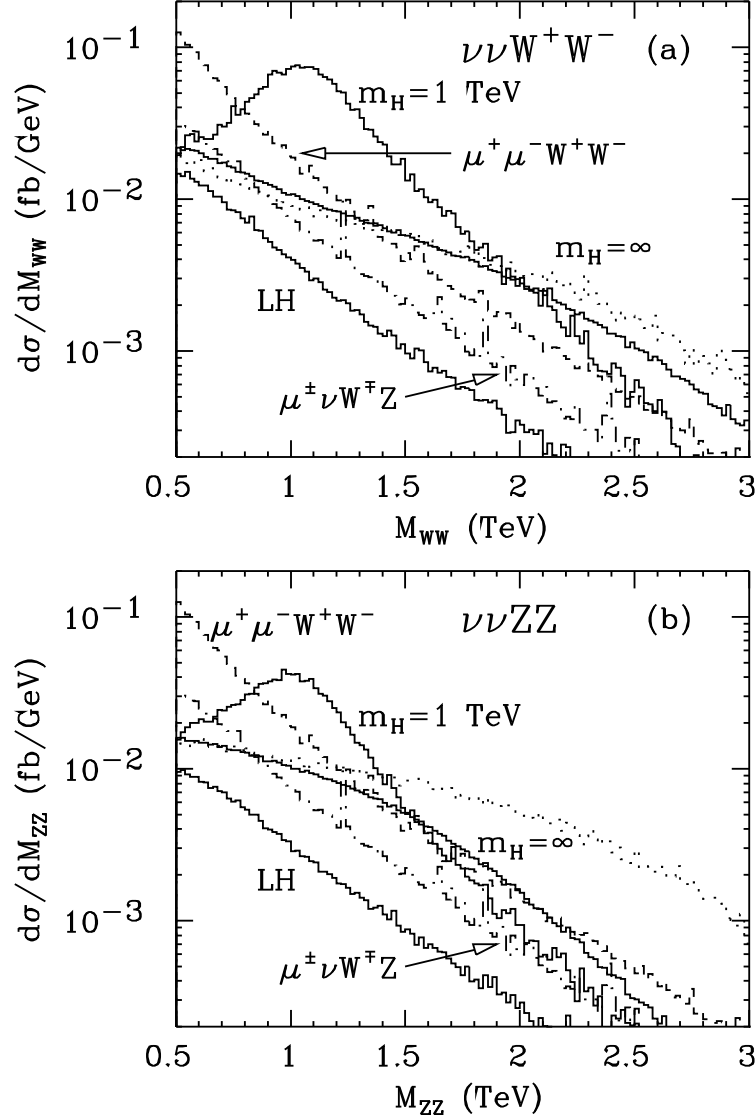


Figure 3: Cross section as a function of M_{VV} for SEWS models and backgrounds at $\sqrt{s} = 4$ TeV in the (a) W^+W^- and (b) ZZ final states after imposing only the basic cuts I. The irreducible background is given by the strictly electroweak LH limit of the Standard Model. The most important reducible backgrounds, $\mu^+\mu^- \rightarrow \mu^+\mu^- W^+W^-$ and $\mu^+\mu^- \rightarrow \mu^\pm \nu W^\mp Z$, are also displayed. The M_{VV} distributions (without subtracting the LH background) for two sample SEWS models are shown: (i) the SM Higgs with $m_H = 1$ TeV; and (ii) the SM with $m_H = \infty$ unitarized via K -matrix techniques (LET-K model). Also shown by the dotted histogram is the $m_H = \infty$ SM result before K -matrix unitarization.

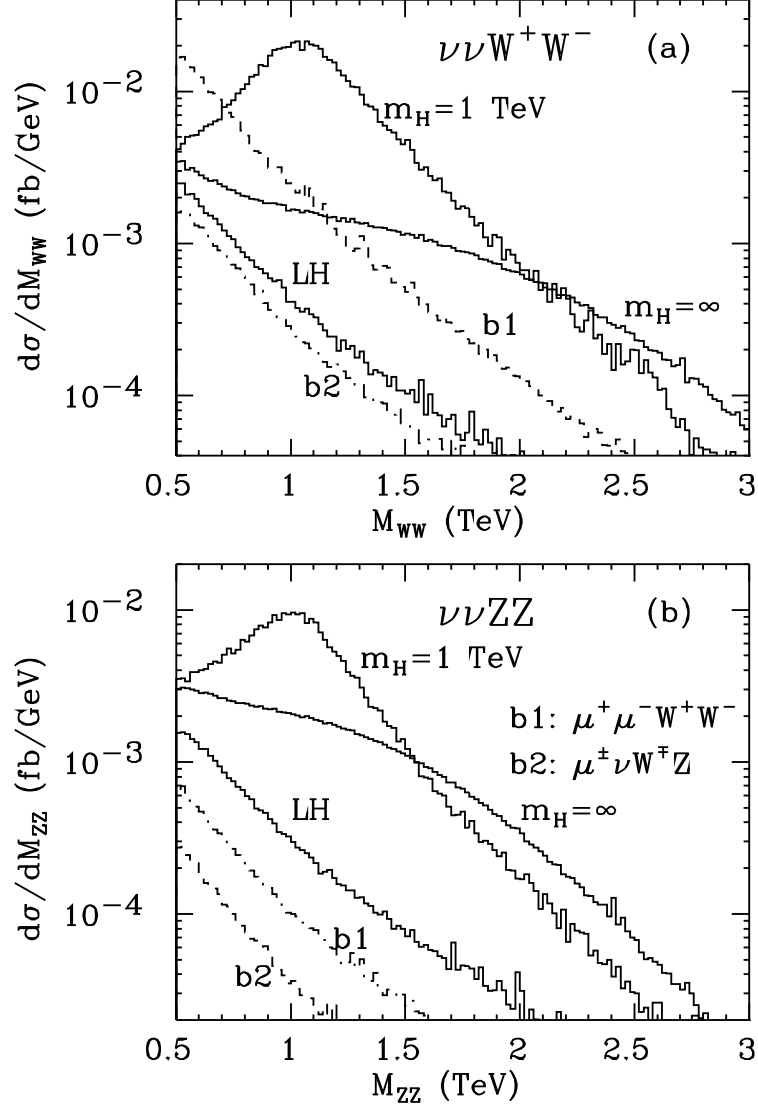


Figure 4: Differential cross sections at $\sqrt{s} = 4$ TeV versus M_{VV} for SEWS models and backgrounds in the (a) W^+W^- and (b) ZZ final states after imposing all cuts I–III. See caption for Fig. 3 for a description of the models.

contribution to the $W^\pm Z$ process, unlike the processes W^+W^- , ZZ . Second, the LET-K $A(s, t, u)$ amplitude goes like t/v^2 which gives a smaller cross section than that of $W^+W^- \rightarrow ZZ$ or $W^+W^+ \rightarrow W^+W^+$ where $A(s, t, u) \propto s/v^2$. Even if there is a T_1 Vector resonance, the W^+W^- final state will reveal a peak with the same strength as does the $W^\pm Z$ final state, with comparable backgrounds from the T_0 and T_2 channels [compare Eqs. (11) and (12)]. Finally, the cuts we have discussed are not as successful for the $W^\pm Z \rightarrow W^\pm Z$ channel. In particular, the $p_T(VV)$ and μ^\pm veto cuts are no longer adequate to substantially suppress the (irreducible) background associated the $W^\pm \gamma \rightarrow W^\pm Z$ subprocess. Highly effective alternative cuts have not yet been identified. (See Ref. [11].)

In Figs. 5a–c we compare the M_{VV} distributions in the W^+W^- , ZZ and W^+W^+ final states for various SEWS models (including the combined reducible and irreducible backgrounds) to those for the combined background with all cuts, I–III, imposed. The SEWS models illustrated are the SM with $m_H = 1$ TeV, the unitarized $m_H = \infty$ (LET-K) model, and a Vector model with $M_V = 2$ TeV and $\Gamma_V = 0.2$ TeV. The numbers in Table 5 are obtained by integrating the distributions in these figures over the specified M_{VV} ranges, where the signal event numbers are those obtained after subtracting the background from the full SEWS model curves (which include the combined background). To indicate the accuracy with which the M_{VV} distributions could be measured, the $L = 200 \text{ fb}^{-1}$, $\pm\sqrt{N}$ error bars associated with several 40 GeV bins for the LET-K model are shown.

From these plots and the sample error bars, it is apparent that, for any of the SEWS models investigated, the expected signal plus background could be readily distinguished from pure background alone on a bin by bin basis at better than 1σ all the way out to $M_{VV} = 2.5$ TeV (2 TeV) in the W^+W^- and W^+W^+ (ZZ) channels. Further, the small 2 TeV Vector model peak would be readily observed in the W^+W^- channel and its absence in the ZZ and W^+W^+ channels would be clear. Indeed, it would be feasible to determine the width of either a scalar or a vector resonance with moderate accuracy.

Currently discussed designs for the 4 TeV muon collider would provide luminosity of $L = 1000 \text{ fb}^{-1}$ per year. Even if this goal is not reached, one might reasonably anticipate accumulating this much luminosity over a period of several years. For $L = 1000 \text{ fb}^{-1}$, the accuracy with which the M_{VV} distributions can be measured becomes very remarkable. To illustrate, we plot in Figs. 6a–b, the signal plus background in

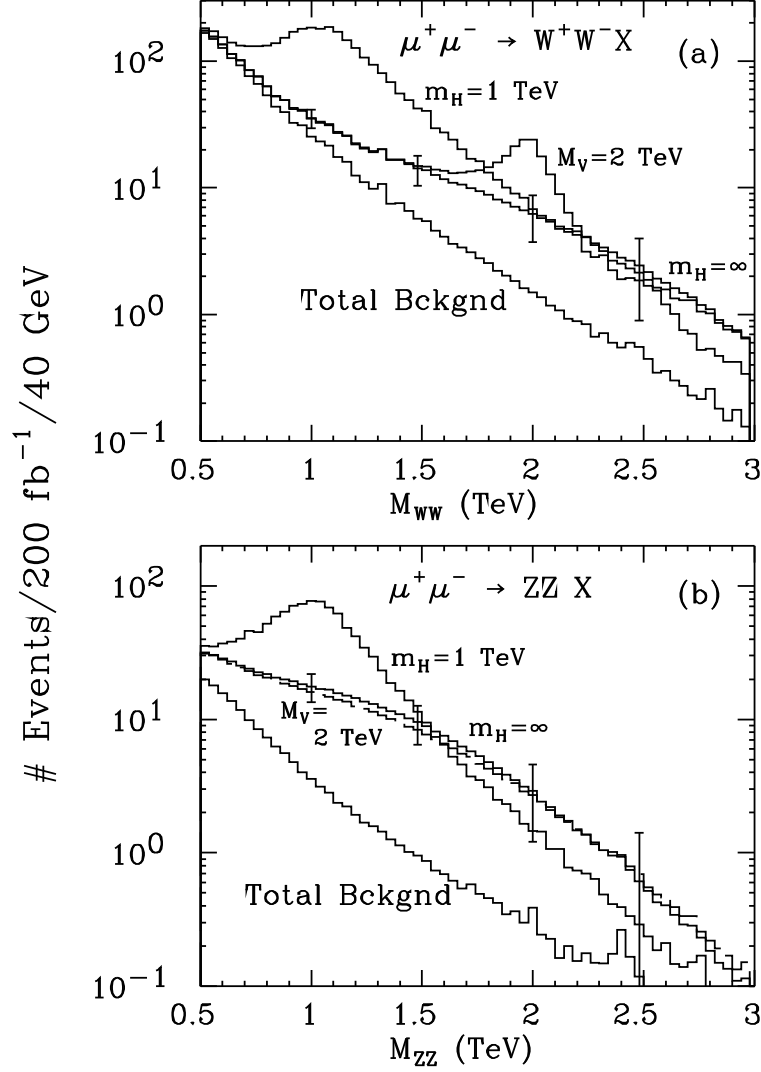


Figure 5: Number of events at $\sqrt{s} = 4$ TeV and $L = 200 \text{ fb}^{-1}$ versus M_{VV} for SEWS models (including the combined backgrounds) and for the combined backgrounds alone in the (a) W^+W^- and (b) ZZ final states after imposing all cuts, I–III. Sample signals shown are: (i) the SM Higgs with $m_H = 1$ TeV; (ii) the SM with $m_H = \infty$ unitarized via K -matrix techniques (LET-K model); and (iii) the Vector model with $M_V = 2$ TeV and $\Gamma_V = 0.2$ TeV. In the ZZ final state the histogram for (iii) falls just slightly lower than that for model (ii) at lower M_{VV} . Sample statistical uncertainties for the illustrated 40 GeV bins are shown in the case of the $m_H = \infty$ model.

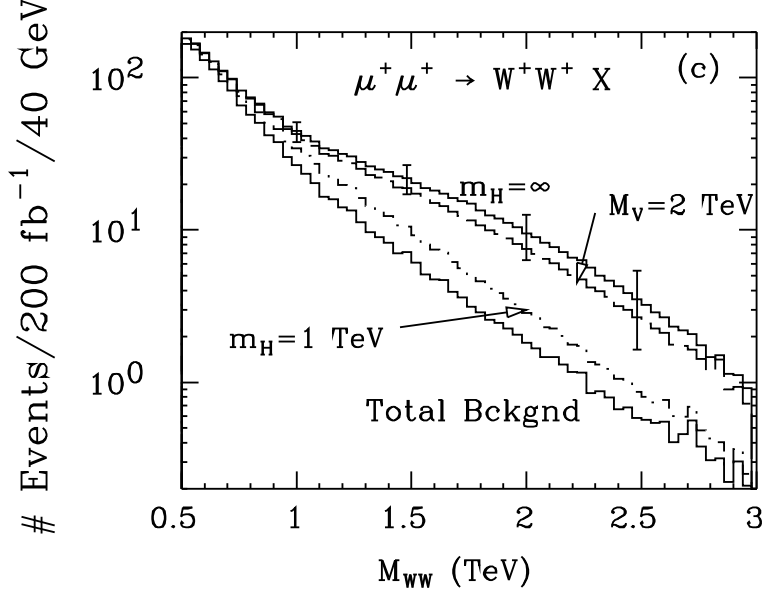


Figure 5: (continued) Events as a function of M_{VV} for sample SEWS models (including the combined backgrounds) and for the combined backgrounds alone in the (c) W^+W^+ final state after imposing all cuts, I–III. See caption for Fig. 5a-b.

the $m_H = 1$ TeV, $\Gamma_H = 0.5$ TeV SM and the $M_S = 1$ TeV, $\Gamma_S = 0.35$ TeV Scalar resonance model, and the combined background, taking $L = 1000$ fb $^{-1}$ and using an 80 GeV bin size (so as to increase statistics on a bin by bin basis compared to the 40 GeV bin size used in the previous figures). The error bars are almost invisible for $M_{VV} \lesssim 1.5$ TeV, and statistics is more than adequate to distinguish between the $\Gamma_H = 500$ GeV SM resonance and a $\Gamma_S = 350$ GeV Scalar model at a resonance mass of 1 TeV. Indeed, we estimate that the width could be measured to better than ± 30 GeV. Further, for such small errors we estimate that a vector resonance could be seen out to nearly $M_V \sim 3$ TeV. This ability to measure the M_{VV} distributions with high precision would allow detailed insight into the dynamics of the strongly interacting electroweak sector. Thus, if some signals for a strongly interacting sector emerge at the LHC, a $\sqrt{s} = 3 - 4$ TeV $\mu^+\mu^-$ (or e^+e^- , if feasible) collider will be essential.

It is important to measure the M_{VV} spectrum in all three (W^+W^- , ZZ and W^+W^+) channels in order to fully reveal the isospin composition of the model. For instance, the Vector model and the LET-K model yield very similar signals in the ZZ and W^+W^+ channels, and would be difficult to separate without the W^+W^- channel

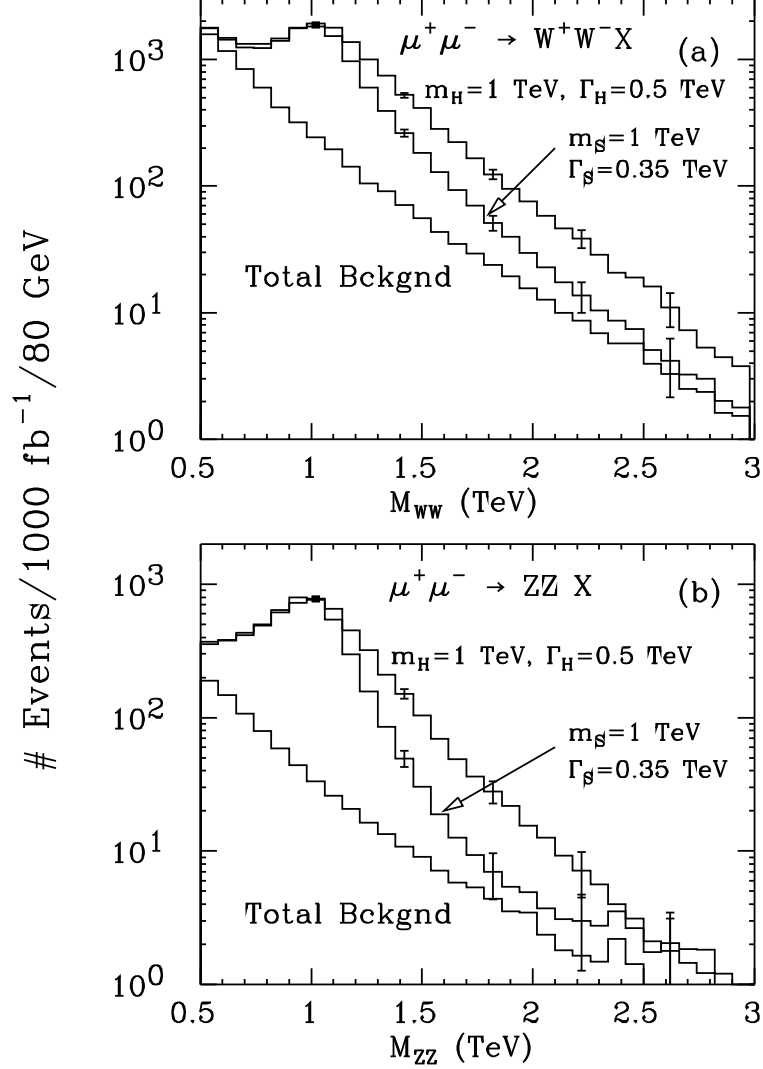


Figure 6: Events versus M_{VV} for two SEWS models (including the combined backgrounds) and for the combined backgrounds alone in the (a) W^+W^- and (b) ZZ final states after imposing all cuts, I–III. Signals shown are: (i) the SM Higgs with $m_H = 1$ TeV, $\Gamma_H = 0.5$ TeV; (ii) the Scalar model with $M_S = 1$ TeV, $\Gamma_S = 0.35$ TeV. Results are for $L = 1000$ fb $^{-1}$ and $\sqrt{s} = 4$ TeV. Sample error bars are shown at $M_{VV} = 1.02, 1.42, 1.82, 2.22$ and 2.62 TeV for the illustrated 80 GeV bins.

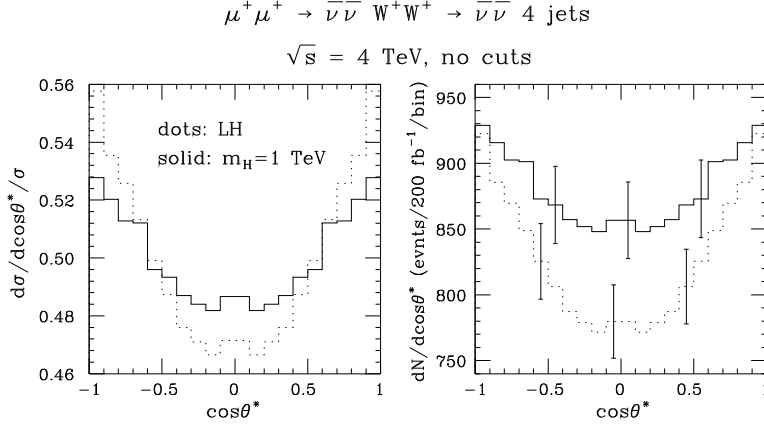


Figure 7: Plots of normalized cross section shapes and $dN/d \cos \theta^*$ (for $L = 200 \text{ fb}^{-1}$) as a function of the $\cos \theta^*$ of the W^+ decays in the $W^+ W^-$ final state. Error bars for a typical $dN/d \cos \theta^*$ bin are displayed. For these two plots no cuts of any kind are performed.

resonance peak. More generally, the ratio of resonance peaks in the ZZ and $W^+ W^-$ channels would be needed to ascertain the exact mixture of Vector (weak isospin 1) and Scalar (isospin 0) resonances should they be degenerate. Determination of the isospin composition of a non-resonant model, such as the LET-K model, requires data from all three channels. The ZZ channel can only be separated from the $W^+ W^-$ channel if the jet energy resolution is reasonably good.

6 SEWS Study using the Projection Procedure

It is advantageous to observe the VV final state in the four-jet mode in order to separate the $V_L V_L$, $V_T V_L$ and $V_T V_T$ final states by angular projection techniques. The angular distributions of interest are those in $\cos \theta_1^*$ and $\cos \theta_2^*$, the cosines of the quark angles in the $V_{1,2}$ rest frames, that we define relative to the boost direction in the $V_1 V_2$ center of mass. Since it is not possible to distinguish quark from antiquark jets in the detector, the configurations

$$[\cos \theta_1^*, \cos \theta_2^*], \quad [-\cos \theta_1^*, \cos \theta_2^*], \quad [\cos \theta_1^*, -\cos \theta_2^*], \quad [-\cos \theta_1^*, -\cos \theta_2^*], \quad (17)$$

must be averaged over. This automatically avoids the problem of the ambiguous sign of $\cos \theta_1^*$ and $\cos \theta_2^*$ in the rest frames of the two V 's. Further, in the $W^+ W^-$ and

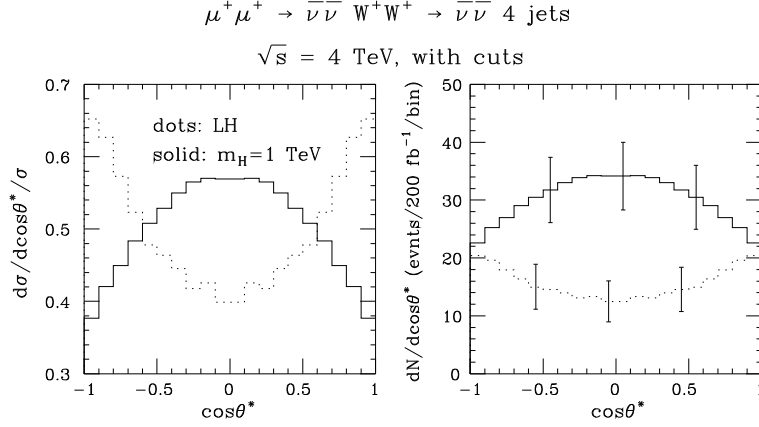


Figure 8: Plots of normalized cross section shapes and $dN/d \cos \theta^*$ (for $L = 200 \text{ fb}^{-1}$) as a function of the $\cos \theta^*$ of the W^+ decays in the W^+W^+ final state. Error bars for a typical $dN/d \cos \theta^*$ bin are displayed. For these two plots we require $M_{VV} \geq 500 \text{ GeV}$, $p_T^V \geq 150 \text{ GeV}$, $|\cos \theta_W^{\text{lab}}| < 0.8$ and $30 \leq p_T^{VV} \leq 300 \text{ GeV}$.

ZZ modes V_1 and V_2 cannot be distinguished; this applies also to the W^+W^- mode in the four-jet final state. Thus, our definition of 1 and 2 is arbitrary, and the above four configurations much be averaged with their $\cos \theta_1^* \leftrightarrow \cos \theta_2^*$ counterparts.

Perhaps typical of the most difficult scenarios would be the $\mu^+\mu^+ \rightarrow W^+W^+\bar{\nu}\bar{\nu}$ channel in the $m_H = 1 \text{ TeV}$ model. As seen in Fig. 5c and discussed with regard to Table 4 the enhancement from strong scattering is quite modest in this case. In this section, we focus on the ability of a projection analysis to discriminate between this SEWS model and the LH background.

Before proceeding with the projection analysis, it is useful to simply examine some typical angular distributions. We construct a one-dimensional ‘average’ $\cos \theta^*$ plot by computing $\cos \theta_1^*$ and $\cos \theta_2^*$ for each event and entering that event at $\cos \theta^* = \cos \theta_1^*$, $-\cos \theta_1^*$, $\cos \theta_2^*$ and $-\cos \theta_2^*$, and dividing by four. In Fig. 7 the normalized shapes $\frac{1}{\sigma} \frac{d\sigma}{d \cos \theta^*}$ and the actual event number distributions $dN/d \cos \theta^*$ (for $L = 200 \text{ fb}^{-1}$) for the LH model and for $m_H = 1 \text{ TeV}$ are compared before applying any cuts. These same distributions are repeated in Fig. 8 after imposing cuts I and II. Even without any cuts, a distinct difference between the $\cos \theta^*$ distributions for the LH model and $m_H = 1 \text{ TeV}$ is observed. The error bars displayed for typical $dN/d \cos \theta^*$ bins make it clear that it would be easy to distinguish the two models from one another using a combination of shape and normalization. After the cuts, designed to enhance the

LL component of the cross section, the shape distributions for the LH model and for $m_H = 1$ TeV are dramatically different. The error bars shown in the $dN/d\cos\theta^*$ plot indicate a discrimination between the two models of very high statistical significance. This will be quantified shortly.

In general, the amplitude as a function of the decay angles of the jets from the two V 's is expressed in terms of a VV helicity amplitude matrix multiplied by appropriate helicity-dependent V decay amplitudes for the jets, summed over helicities. If the azimuthal angles of the jets in the rest frames of the two V 's are integrated over, then the amplitude squared diagonalizes yielding an expression of the form:

$$\frac{d\sigma}{d\cos\theta_1^* d\cos\theta_2^*} \equiv \Sigma(\cos\theta_1^*, \cos\theta_2^*) = \sum_{ij} \rho_{ij} f_i(\cos\theta_1^*) f_j(\cos\theta_2^*), \quad (18)$$

where we have suppressed all kinematical variables except $\cos\theta_1^*$ and $\cos\theta_2^*$. In Eq. (18), the i, j indices are summed over $+$, $-$, and L , and $f_+(z) \propto (1+z)^2$, $f_-(z) \propto (1-z)^2$, and $f_L(z) \propto (1-z^2)$.

Because of our inability to distinguish quarks from and antiquarks, we must bin in $\cos\theta_1^*$ and $\cos\theta_2^*$ by entering the weight for each event in the four bins specified in Eq. (17). This results in a simplification due to the fact that $f_+(z) + f_+(-z) = f_-(z) + f_-(-z) \propto 1+z^2$; $f_L(z)$ is not altered. After symmetrizing over $\cos\theta_1^* \leftrightarrow \cos\theta_2^*$ (due to our inability to distinguish V_1 from V_2), the final form for the cross section as a function of $\cos\theta_1^*$ and $\cos\theta_2^*$ in the ZZ , W^+W^- or W^+W^+ channels is

$$\begin{aligned} \Sigma(\cos\theta_1^*, \cos\theta_2^*) &= \sigma_{TT} f_{TT}(\cos\theta_1^*, \cos\theta_2^*) + \sigma_{LL} f_{LL}(\cos\theta_1^*, \cos\theta_2^*) \\ &+ \sigma_{TL} f_{TL}(\cos\theta_1^*, \cos\theta_2^*), \end{aligned} \quad (19)$$

where

$$\begin{aligned} f_{TT} &= f_T(\cos\theta_1^*) f_T(\cos\theta_2^*), \quad f_{LL} = f_L(\cos\theta_1^*) f_L(\cos\theta_2^*), \\ f_{TL} &= \frac{1}{2} [f_T(\cos\theta_1^*) f_L(\cos\theta_2^*) + f_L(\cos\theta_1^*) f_T(\cos\theta_2^*)], \end{aligned} \quad (20)$$

with

$$f_L(z) \equiv \frac{3}{4}(1-z^2), \quad f_T(z) = \frac{3}{8}(1+z^2); \quad (21)$$

the normalizations are chosen so that $\int_{-1}^{+1} f_i(z) dz = 1$. With this normalization, the $\sigma_{LL,TT,TL}$ are the cross sections for LL, TT, TL final states integrated over all of VV

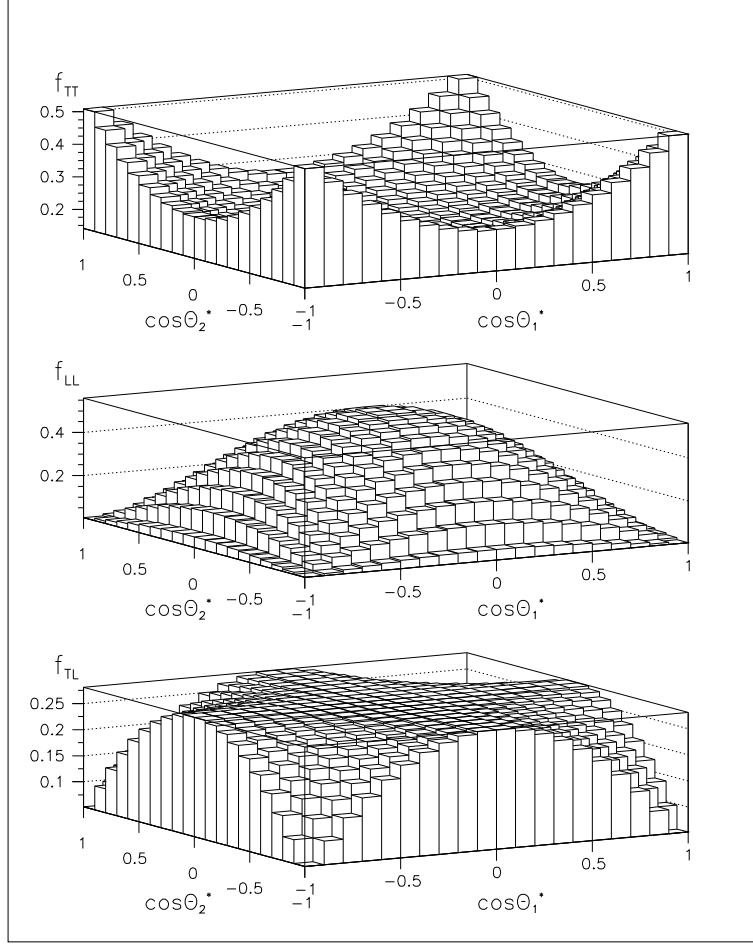


Figure 9: The functions $f_{TT}(\cos \theta_1^*, \cos \theta_2^*)$, $f_{LL}(\cos \theta_1^*, \cos \theta_2^*)$ and $f_{TL}(\cos \theta_1^*, \cos \theta_2^*)$ [see Eq. (20)] are plotted as a function of $\cos \theta_1^*$ and $\cos \theta_2^*$ in two-dimensional parameter space.

phase space (subject to cuts). Thus, after integrating $\Sigma(\cos \theta_1^*, \cos \theta_2^*)$ over $\cos \theta_1^*$ and $\cos \theta_2^*$, the total cross section is given by

$$\sigma_{\text{tot}} = \sum_{i=TT,TL,LL} \sigma_i \equiv \sigma_{TT} + \sigma_{TL} + \sigma_{LL} . \quad (22)$$

For later reference, the three functions of Eq. (20) are plotted in the two-dimensional $\cos \theta_1^*, \cos \theta_2^*$ parameter space in Fig. 9. The goal of the projection analysis is to determine the coefficients of these three distinct two-dimensional distributions within a set of data that contains an unknown mixture of them.

The optimal projection procedure (see Ref. [12]) is to compute the matrix

$$M_{ij} \equiv \int \frac{f_i(\cos \theta_1^*, \cos \theta_2^*) f_j(\cos \theta_1^*, \cos \theta_2^*)}{\Sigma(\cos \theta_1^*, \cos \theta_2^*)} d \cos \theta_1^* d \cos \theta_2^*, \quad i, j = TT, LL, TL, \quad (23)$$

and the integrals

$$I_i \equiv \int f_i(\cos \theta_1^*, \cos \theta_2^*) d \cos \theta_1^* d \cos \theta_2^*, \quad (24)$$

using the known f_i and the experimentally measured Σ , where the integrals are taken over $\cos \theta_1^*, \cos \theta_2^*$. The I_i are equal to 1 in our normalization. The coefficients σ_i are then determined as:[‡]

$$\sigma_i = \sum_j M_{ij}^{-1} I_j = \sum_j M_{ij}^{-1}, \quad i, j = TT, LL, TL. \quad (25)$$

The above formulae assume that cuts are performed only on the V 's and not on their jet decay products. If significant cuts are performed on the jets then the procedure becomes more subtle since the $\cos \theta_1^*$ and $\cos \theta_2^*$ dependence no longer necessarily factors from dependence on the other kinematical variables. The generalization is a well-defined extension of that discussed above [12]. We expect that the experimentally required jet cuts will not significantly alter the results we shall obtain without jet cuts, provided that the jet cuts are mild. The analysis does become model-dependent if there are strong correlations between other kinematic variables (especially M_{VV}) and the ranges of $\cos \theta_1^*$ and $\cos \theta_2^*$ that are accepted.

The expected experimental statistical errors in the projection determinations of the σ_i for a given model are determined in terms of the covariance matrix $\langle \Delta \sigma_i \Delta \sigma_j \rangle$ defined by

$$V_{ij} \equiv \langle \Delta \sigma_i \Delta \sigma_j \rangle = \frac{M_{ij}^{-1} \sigma_{\text{tot}}}{N}, \quad (26)$$

where σ_{tot} is defined in Eq. (22), N is the total number of events expected (after cuts), and M_{ij} is computed from Eq. (23) using the model prediction for $\Sigma(\cos \theta_1^*, \cos \theta_2^*)$.

Let us suppose that the model predicts values σ_i^0 for the three coefficients. (Note that the coefficient σ_{TT}^0 for any SEWS model is that predicted in the light Higgs SM.) In a real experiment, Eq. (25) would yield values σ_i^* that are close to the σ_i^0 , and we would then want to draw confidence-level ellipsoids about the σ_i^* . We can approximate this procedure by assuming a given input model with corresponding predictions for

[‡]Here, and in all subsequent equations, the notation X_{ij}^{-1} , where X is any matrix, refers to the i, j component of the inverse matrix, X^{-1} .

the σ_i^0 and then compute the $\Delta\chi^2$ that would be associated with values of the σ_i that differ from the input σ_i^0 :

$$\Delta\chi^2 = \sum_{i,j} (\sigma_i - \sigma_i^0)(\sigma_j - \sigma_j^0) V_{ij}^{-1}, \quad \text{with } V_{ij}^{-1} = \frac{M_{ij}N}{\sigma_{\text{tot}}}, \quad (27)$$

where, as above, $i, j = TT, LL, TL$. The confidence-level, $CL(\Delta\chi^2)$ at which a fixed $\Delta\chi^2$ ellipsoid can be said to contain the true values of the σ_i is then given in terms of the cumulative distribution function F (see Ref. [13], Eq. (16.22)) by

$$1 - CL(\Delta\chi^2) = F(\Delta\chi^2, n), \quad (28)$$

where n is the number of parameters: $n = 3$ if all three σ_i are being considered. If we are primarily interested in the TT and LL coefficients, as will be case in the model considered in detail below, the correct procedure is to take the $i, j = TT, LL$ submatrix of the covariance matrix $V_{ij} = M_{ij}^{-1}$, invert it and apply Eq. (27) in the TT, LL ($n = 2$) parameter subspace. The 68.3% and 90% confidence-level ellipses in this two parameter subspace are then defined by $\Delta\chi^2 = 2.295$ and $\Delta\chi^2 = 4.606$, respectively. The usual 1σ or 68.3% confidence-level error on any one parameter σ_i without regard to other parameters is obtained by the one-parameter version of the above procedure, and corresponds to $\Delta\chi^2 = 1$, yielding

$$\Delta\sigma_i = [M_{ii}^{-1}\sigma_{\text{tot}}/N]^{1/2}. \quad (29)$$

Below, we discuss only $\Delta\sigma_i$ as defined above, but when the experiment is actually performed it will be highly desirable to construct the CL ellipsoids.[§] We now analyze how successful this procedure can be in practice.

Let us turn to the full two-dimensional projection analysis. The challenge is illustrated in Fig. 10. There we plot the Monte Carlo prediction for $\frac{1}{\sigma_{\text{tot}}} \frac{d\sigma}{d\cos\theta_1^* d\cos\theta_2^*}$ as a function of $\cos\theta_1^*$ and $\cos\theta_2^*$ for the LH model and for $m_H = 1$ TeV, both before any cuts and after cuts I and II on the W^+ 's. Fluctuations in this figure are purely a result of the Monte Carlo statistics, and are not meant to reflect actual statistical errors in a typical experiment. For the LH model and no cuts, the Monte Carlo generated distribution mainly follows the expectations for f_{TT} (see Fig. 9). For

[§]We note that the errors obtained in the projection formalism closely approximate those that would result using a χ^2 minimization procedure in the σ_i for a given known form of $\Sigma(\cos\theta_1^*, \cos\theta_2^*)$ as a function of the σ_i .

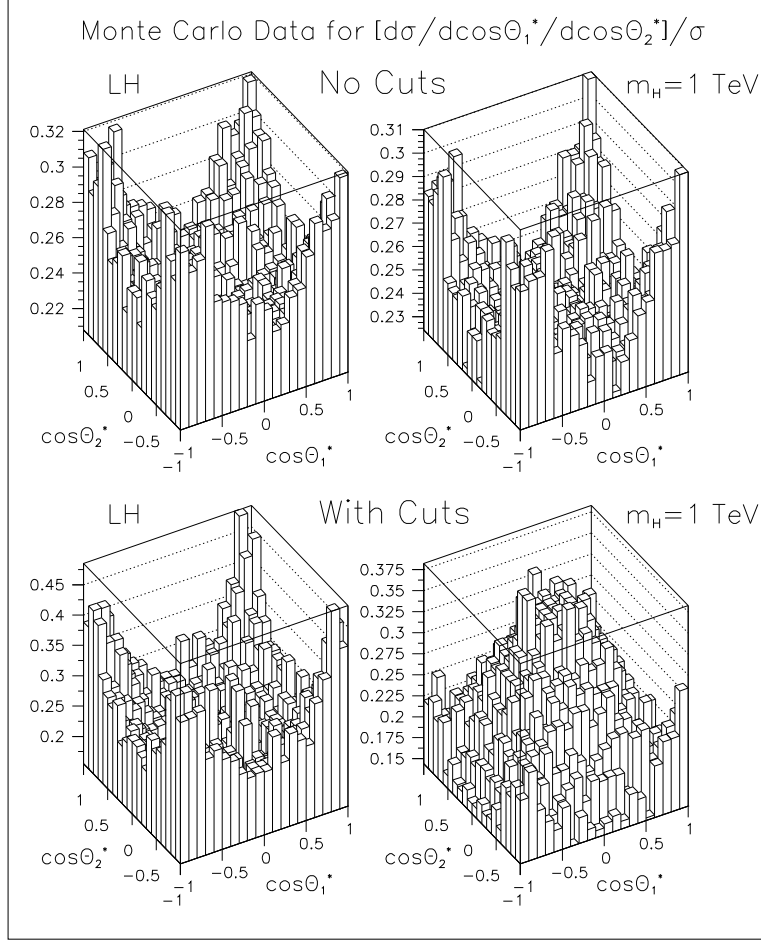


Figure 10: Monte Carlo generated prediction for $\frac{1}{\sigma_{\text{tot}}} \frac{d\sigma}{d\cos\theta_1^* d\cos\theta_2^*}$ in the W^+W^+ channel at $\sqrt{s} = 4$ TeV in the two-dimensional $\cos\theta_1^*, \cos\theta_2^*$ space for four cases: (i) LH, no cuts; (ii) $m_H = 1$ TeV, no cuts; (iii) LH, with cuts I and II; (iv) $m_H = 1$ TeV, with cuts I and II.

$m_H = 1$ TeV and no cuts, it is possible to observe some extra structure in the vicinity of $\cos \theta_1^* \sim \cos \theta_2^* \sim 0$ coming from a f_{LL} component. The one-dimensional projection of these two-dimensional distributions, as plotted in Fig. 7, makes this difference clear. After imposing cuts I and II, Fig. 10 shows a dramatic difference between the LH and $m_H = 1$ TeV models, with the latter being heavily dominated by the f_{LL} type of structure – the f_{TT} component is mainly apparent in the enhancements at the $|\cos \theta_1^*| = |\cos \theta_2^*| = 1$ corners. Hence, our two-dimensional projection will discriminate between the LH and $m_H = 1$ TeV models at a very high level of statistical significance if (after cuts are imposed) there are enough experimental events that the actual data resembles the Monte Carlo prediction.

Table 6: Percentage contributions of the TT , TL and LL W^+W^+ final states, for the LH and $m_H = 1$ TeV Standard Model cases at $\sqrt{s} = 4$ TeV, as computed theoretically and as obtained from the projection analysis.

	LH			$m_H = 1$ TeV		
	TT	TL	LL	TT	TL	LL
Theory/No Cuts	59.2%	32.6%	8.2%	56.2%	30.1%	13.7%
Projection/No Cuts	59.4%	32.3%	8.3%	56.7%	29.1%	14.2%
Theory/With Cuts	85.9%	12.2%	1.9%	45.0%	5.0%	50.0%
Projection/With Cuts	87.0%	9.8%	3.2%	47.6%	-1.3%	53.4%

To test our projection analysis we have applied the projection techniques outlined earlier to the (somewhat imperfect) Monte Carlo generated distributions of Fig. 10 (before dividing by σ_{tot}). In Table 6 we give the percentage contribution to the integrated cross section deriving from TT , TL and LL final states both before and after the cuts I and II, comparing results for the LH case to $m_H = 1$ TeV. These percentages are simply computed from the numbers in Table 4, which were obtained by manually inserting the appropriate polarization projectors into the Monte Carlo matrix elements. Also presented in Table 6 are these same percentages *as extracted from the Monte Carlo generated distributions following the projection procedure outlined above*. There is excellent agreement, except for the polarization combination TL when it is a very small fraction of the total cross section. The success of the procedure is quite remarkable given the substantial fluctuations in the Monte Carlo distributions (Fig. 10) that we input. In particular, the projection procedure is suc-

successful in demonstrating that the cross section increase in going from the LH case to $m_H = 1$ TeV is primarily in the LL mode, *even in the case where no cuts are applied*. It is important to note that the differences between the ‘Theory’ and ‘Projection’ results in Table 6 are purely those related to the limited accuracy of our Monte Carlo integrations and have nothing to do with experimental errors.

Table 7: Relative 1σ statistical errors, $\Delta\sigma_i/|\sigma_i|$ ($i = TT, TL, LL$), expected for the projection technique in the W^+W^+ channel for the $m_H = 1$ TeV SEWS model, assuming $L = 200 \text{ fb}^{-1}$ at $\sqrt{s} = 4$ TeV.

	LH			$m_H = 1$ TeV		
	TT	TL	LL	TT	TL	LL
Projection/No Cuts	0.04	0.11	0.22	0.04	0.12	0.13
Projection/With Cuts	0.21	4	3	0.22	13	0.17

In order to determine the relative (1σ) statistical errors expected for the different cross section components when employing the projection technique to real experimental data, we calculate $\Delta\sigma_i/|\sigma_i|$ with $\Delta\sigma_i$ using Eq. (29) with N as predicted for $L = 200 \text{ fb}^{-1}$ and using the exactly computed M_{ij} for the model in question. These relative errors are presented in Table 7. For those cross section components that are a substantial fraction of the total, the relative statistical errors are quite good. They would be a factor of 2.23 better for $L = 1000 \text{ fb}^{-1}$. We give a few examples:

- For $L = 200 \text{ fb}^{-1}$, the 2σ upper limit on σ_{LL} [see Eq. (22)] for no cuts (cuts) and the LH model is 7.86 fb (0.24 fb) while the 2σ lower limit on σ_{LL} for no cuts (cuts) and $m_H = 1$ TeV is 8.76 fb (1.0 fb).
- In the cuts case, for $L = 200 \text{ fb}^{-1}$, the 4σ upper limit on σ_{LL} for the LH model is 0.48 fb and the 4σ lower limit on σ_{LL} for $m_H = 1$ TeV is also 0.48 fb.

Thus, especially by applying cuts, a high level of statistical discrimination between the $m_H = 1$ TeV and the LH models is possible. We re-emphasize that this is one of the most difficult cases that we could have considered. Statistical discrimination for most other models and channels would be very dramatic indeed.

In order to obtain a more detailed picture of the SEWS model function $A(s, t, u)$ defined earlier, it would be very advantageous if the above analysis could be applied

on a bin-by-bin basis as a function of M_{VV} . For $m_H = 1$ TeV in the W^+W^+ channel, we estimate that the minimum bin size needed to retain adequate statistics for $M_{VV} \lesssim 2$ TeV in the projection analysis at $L = 1000 \text{ fb}^{-1}$ is ~ 250 GeV. Further work on this type of analysis is in progress.

It is important to assess the impact of a realistic experimental detector environment upon the projection procedure. Since this is highly detector dependent, we only make some general comments.

- Jet cuts should not greatly decrease the viability of the projection procedure. If there is significant distortion due to the non-factorization of $\cos \theta_1^*$ and $\cos \theta_1^*$ dependencies from other kinematical variables, then the generalized procedure (discussed in general terms in [12]) must be followed, and the extraction of the σ_i would become somewhat model-dependent.
- We have investigated the extent to which smearing of the jet energies results in a deterioration of the procedure. This can affect the experimental determination of $\cos \theta_1^*$ and $\cos \theta_2^*$ because the smearing is in the laboratory frame and the smeared momenta are then used to determine the boosts required to go to the W^+W^+ rest frame and then to the individual W^+ rest frames where the angles are ultimately defined. For jet energy resolution of order $\Delta E/E \sim 50\%/\sqrt{E} \oplus 2\%$, the effect is smaller than the Monte Carlo statistics that we were able to achieve in our program.
- An important experimental issue is the ability of the detector to properly resolve the two jets coming from a given W^+ . On the average, they are separated at $\sqrt{s} = 4$ TeV by about 17° in the laboratory. The detector must be designed with this in mind. Failure to achieve good separation of the two jets would mean that the projection procedure could not be employed. Detectors being discussed will have sufficient segmentation that good separation should be possible.
- A closely related issue is the uncertainty in the experimental determination of the angles of the jets in the laboratory frame. Errors in these angles could possibly lead to a distortion in the determination of $\cos \theta_1^*$ and $\cos \theta_2^*$ that is larger than that from simple energy smearing.

Because the last two items are so detector dependent, we have not attempted a detailed study.

7 Summary and Conclusion

Achieving VV scattering subprocess energies above $1-2$ TeV is critical for studies of strongly interacting electroweak sector (SEWS) models, and is only possible with high event rates at lepton-antilepton (e^+e^- or $\mu^+\mu^-$ colliders) or quark-antiquark (hadron collider) subprocess energies of order $3-4$ TeV. Consequently, a muon collider facility with center of mass energy $\sqrt{s} \sim 3-4$ TeV and luminosity $L = 200-1000 \text{ fb}^{-1}$ allowing both $\mu^+\mu^-$ and $\mu^+\mu^+$ (or $\mu^-\mu^-$) collisions would be a remarkably powerful machine for probing a strongly interacting electroweak sector (SEWS). The LHC or a lower energy e^+e^- collider would not be competitive.

Event rates for even the weakest of the model signals studied are such that the M_{VV} distributions could be quantitatively delineated, thereby providing a direct measurement of the underlying strong VV interaction amplitude as a function of the VV subprocess energy and strong differentiation among various possible models of the strongly interacting electroweak sector.

Statistics are even sufficient that a model-independent projection analysis can be applied to M_{VV} integrated data (either before or after cuts) to isolate the TT , TL and LL components of the cross section. Employing the projection techniques with acceptance cuts imposed to extract the LL component of the W^+W^+ cross section, for $L = 200 \text{ fb}^{-1}$ we found that the 4σ statistical upper limit for the light Higgs Standard Model prediction is slightly lower than the 4σ lower limit for the $m_H = 1$ TeV result. This level of statistical discrimination between the models is remarkable, considering that the $m_H = 1$ TeV cross section in the W^+W^+ channel is one of the most difficult channels and models for isolating the LL cross section. For most SEWS models, the statistical level at which a model-independent extraction of the LL cross section could be demonstrated to be inconsistent with the light Higgs Standard Model expectation would be much larger. Comparison of LL cross sections in the W^+W^- , ZZ and W^+W^+ final states with one another and with model expectations would single out a small class of viable SEWS theories. We are optimistic that the LL cross section could be extracted for many SEWS models and channels even on a bin-by-bin basis in M_{VV} , with a model and channel dependent bin size of order 250 GeV (in the range $M_{VV} \lesssim 2 \text{ TeV}$), if $L = 1000 \text{ fb}^{-1}$ of data is available. This would further delineate the correct theory underlying the strong electroweak interactions.

Thus, if evidence for a strongly interacting electroweak sector emerges from LHC

or NLC data, construction of a high luminosity, high energy muon collider (or electron collider, if feasible) should be given the highest priority.

ACKNOWLEDGMENTS

This work was supported in part by the U.S. Department of Energy under Grants No. DE-FG02-95ER40896, No. DE-FG03-91ER40674 and No. DE-FG02-91ER40661. Further support was provided by the University of Wisconsin Research Committee, with funds granted by the Wisconsin Alumni Research Foundation, and by the Davis Institute for High Energy Physics.

APPENDIX

K-matrix Unitarization for *WW* scattering Amplitudes

WW scattering amplitudes in SEWS models violate unitarity at high energies, especially for the non-resonant scattering, such as *ZZ* and *W⁺W⁺*, final states. One therefore must unitarize them in some specific scheme to obtain physical results. For simplicity, we have taken the *K*-matrix unitarization scheme [14]. Namely, for a given partial wave amplitude, a_l , we unitarize it by the following replacement:

$$a_l \rightarrow \frac{a_l}{1 - ia_l}. \quad (\text{A.1})$$

The partial wave amplitude a_l before the unitarization is obtained from the isospin amplitudes T_I ,

$$a_l^I = \frac{1}{64\pi} \int_{-1}^1 d\cos\theta P_l(\cos\theta) T_I. \quad (\text{A.2})$$

In turn, T_I is given by the fundamental amplitude function $A(s, t, u)$ as discussed in Sec.2.

Inversely,

$$T_I = 32\pi \sum_{l=0}^{\infty} (2l+1) P_l(\cos\theta) a_l^I. \quad (\text{A.3})$$

Applying Eq. (A.1) to a_l^I , the amplitudes T_I and the physical scattering amplitudes in Eqs. (10)-(13) are thus unitarized.

7.1 Unitarization of LET amplitudes

The fundamental amplitude function $A(s, t, u)$ according to the low energy theorem is given by

$$A(s, t, u) = s/v^2. \quad (\text{A.4})$$

Before the unitarization, the T_I 's are

$$T_0 = \frac{2s}{v^2}, \quad T_1 = \frac{s}{v^2} \cos \theta, \quad T_2 = -\frac{s}{v^2}, \quad (\text{A.5})$$

where $\cos \theta = (t - u)/s$. Correspondingly,

$$a_0^{I=0} = \frac{1}{16\pi} \frac{s}{v^2}, \quad a_1^{I=1} = \frac{1}{96\pi} \frac{s}{v^2}, \quad a_0^{I=2} = -\frac{1}{32\pi} \frac{s}{v^2}. \quad (\text{A.6})$$

Inversely from Eq. (A.3),

$$T_0 = 32\pi a_0^{I=0}, \quad T_1 = 96\pi a_1^{I=1} \cos \theta, \quad T_2 = 32\pi a_0^{I=2}. \quad (\text{A.7})$$

The amplitudes are thus unitarized by applying Eq. (A.1) to a_l^I .

7.2 Unitarization for the Vector Model

We now present the unitarization procedure in the Vector Model for the non-resonant channels

$$W^+W^- \rightarrow ZZ, \quad \text{and} \quad W^+W^+ \rightarrow W^+W^+. \quad (\text{A.8})$$

The fundamental amplitude function $A(s, t, u)$ in the Vector Model is given by [2]

$$A(s, t, u) = \frac{s}{4v^2}(4 - 3\alpha) + \frac{\alpha M_V^2}{4v^2} \left(\frac{u - s}{t - M_V^2} + \frac{t - s}{u - M_V^2} \right). \quad (\text{A.9})$$

where α is a model parameter [2]. We need only T_0 and T_2 to evaluate the scattering amplitudes of Eq. (A.8) and we find that

$$T_0 = 2A(s, t, u), \quad T_2 = -A(s, t, u). \quad (\text{A.10})$$

If we assume s -wave dominance, then the $l = 0$ partial wave amplitudes can be expressed as

$$a_0^{I=0} = \frac{1}{16\pi} \frac{s}{v^2} F(\alpha, M_V^2, s), \quad a_0^{I=2} = -\frac{1}{32\pi} \frac{s}{v^2} F(\alpha, M_V^2, s), \quad (\text{A.11})$$

where

$$F(\alpha, M_V^2, s) = 1 - \frac{\alpha}{2} \left(\frac{3}{2} + \frac{M_V^2}{s} \right) + \frac{\alpha}{2} \left(2 + \frac{M_V^2}{s} \right) \frac{M_V^2}{s} \ln \left(1 + \frac{s}{M_V^2} \right). \quad (\text{A.12})$$

With the relations in Eq. (A.7), the amplitudes can be unitarized by applying Eq. (A.1) to a_l^I in Eq. (A.11).

REFERENCES

1. D. A. Dicus and V. S. Mathur, Phys. Rev. **D7**, 3111 (1973); B. W. Lee, C. Quigg, and H. Thacker, Phys. Rev. **D16**, 1519 (1977); M. Veltman, Acta Phys. Polon. **B8**, 475 (1977); M. S. Chanowitz and M. K. Gaillard, Nucl. Phys. **B261**, 379 (1985).
2. J. Bagger, V. Barger, K. Cheung, J.F. Gunion, T. Han, G.A. Ladinsky, R. Rosenfeld, and C.-P. Yuan, Phys. Rev. **D49**, 1246 (1994); *ibid.* **D52**, 3878 (1995).
3. V. Barger *et al.*, Phys. Rev. **D42**, 3052 (1990); V. Barger *et al.*, Phys. Rev. **D44**, 1426 (1991); *ibid.* Phys. Rev. **D44**, 2701 (1991); D. Dicus, J. Gunion, and R. Vega, Phys. Lett. **B258**, 475 (1991); M. Berger and M. Chanowitz, Phys. Lett. **B263**, 509 (1991); D. Dicus *et al.*, Nucl. Phys. **B377**, 31 (1992); M. S. Chanowitz and W. Kilgore, Phys. Lett. **B322**, 147 (1994); *ibid.* **B347**, 387 (1995).
4. ATLAS Collaboration, Technical Proposal, CERN/LHCC/94-13; ATLAS Internal Note PHYS-NO-033; CMS Collaboration, Technical Proposal, CERN/LHCC/94-38.
5. V. Barger, K. Cheung, T. Han, and R.J.N. Phillips, Phys. Rev. **D52**, 3815 (1995).
6. J. Gunion and A. Tofghi-Niaki, Phys. Rev. **D36**, 2671 (1987); *ibid.* **D38**, 1433 (1988); K. Hagiwara, J. Kanzaki and H. Murayama, KEK-TH-282 (1991); V. Barger, K. Cheung, B.A. Kniehl and R.J.N. Phillips, Phys. Rev. **D46**, 3725 (1992); Y. Kurihara and R. Najima, Phys. Lett. **B301**, 292 (1993).
7. E. Eichten, I. Hinchliffe, K. Lane and C. Quigg, Phys. Rev. **D34**, 1547 (1986); K. Lane, BUHEP-94-2, 1993 TASI Lectures (World Scientific), and references therein.
8. A. Dobado, M. J. Herrero, J. Terron, Z. Phys. **C50**, 465 (1991); R. Casalbuoni *et al.*, Phys. Lett. **B249**, 130 (1990); hep-ph/9502325 (Aug. 1994).
9. T. Barklow, in the Albuquerque DPF94 Meeting, ed. by Sally Seidel, p. 1236, and references therein.
10. D. Burke, *Proceedings of the Symposium on Physics Potential and Development of $\mu^+\mu^-$ Colliders*, San Francisco, California, December 13-15, 1995.
11. Y. Kurihara and R. Najima, KEK-PREPRINT-93-90; and in *Proceedings of the fourth workshop on Japan Linear Collider*, KEK Proceedings 94-1, p.20, ed. Y. Kurihara.
12. J.F. Gunion, B. Grzadkowski, X.-G. He, UCD-96-14.
13. Particle Data Group, L. Montanet *et al.*, Phys. Rev. **D50**, 1173 (1994).
14. For a review of unitarization schemes, see *e.g.* K.-I. Hikasa, in *Physics and Experiments with Linear Colliders*, Saariselka, Finland, September 1992, ed. R. Orava *et al.*, World Scientific, p. 451.